Eurasia Journal of Science and Technology
Print ISSN: 2663-1024
Online ISSN: 2663-1016
DOI: https://doi.org/10.61784/ejst3141

ENZYME-FREE COLOURIMETRIC SENSOR BASED ON ZIRCONIUM-BASED MOF FOR THE DETECTION OF MALATHION

Rui Liu[1,2], WenJia Chen[1,2], JunXian Li[1,2], Run Wang[1,2], Liang Dong[1,2*]
[1]*School of Food and Liquor Engineering, Sichuan University of Science and Engineering, Yibin 644000, Sichuan, China.*
[2]*The Liquor Making Biological Technology & Application of Key Laboratory of Sichuan Province, Yibin 644000, Sichuan, China.*
[*]*Corresponding Author: Liang Dong*

Abstract: To address the issues of enzyme inactivation, complex procedures, and dependence on large-scale equipment in traditional organophosphorus pesticide detection, we developed an enzyme-free colourimetric sensor employing Hemin@UiO-66 composite nanomaterials for the rapid and accurate detection of malathion. The UiO-66 metal-organic framework was synthesised using the solvothermal method, while the Hemin@UiO-66nanoenzyme was produced through post-modification with hemin chloride (Hemin). The structural characteristics of the material were analysed using Fourier transform infrared spectroscopy (FT-IR), X-ray diffraction (XRD), scanning electron microscopy (SEM), and X-ray photoelectron spectroscopy (XPS).Thisnanoenzyme demonstrated remarkable peroxidase-like activity, effectively catalysing the oxidation of 3,3',5,5'-tetramethylbenzidine (TMB) to blue-coloured oxidised TMB (oxTMB) in the presence of hydrogen peroxide (H_2O_2). Malathion interacts with the active sites of the material via Zr-O-P coordination, which significantly inhibits the catalytic activity of thenanoenzyme. As a result, the colour of the system gradually diminished with increasing malathion concentration. Under optimised conditions, a strong linear correlation was established between the change in absorbance of the sensor and malathion concentration, spanning from 5 to 270 ng/mL, with a detection limit as low as 4.23 ng/mL (3σ) and a detection time of 20 minutes. This method exhibited excellent selectivity, stability, repeatability, and anti-interference capabilities. The recovery rates of malathion in spiked real samples ranged from 95.3% to 104.7%, accompanied by a relative standard deviation (RSD) of less than 4.2%. By eliminating the need for biological enzymes, this sensor facilitates straightforward operation and rapid response, thereby providing an innovative approach for the on-site rapid detection of malathion residues in food.
Keywords: Zirconium-based MOF; Nanoenzyme; Enzyme-free colourimetric sensor; Malathion

1 INTRODUCTION

Organophosphorus pesticides are widely employed in agriculture due to their potent insecticidal and bactericidal properties [1-3]. Among these, malathion is a broad-spectrum organophosphorus insecticide that is particularly common in the management of diseases and pests affecting crops such as fruits, vegetables, and grains [4, 5]. However, the excessive application and inadequate management of malathion residues can result in its accumulation in the human body through the food chain. This accumulation inhibits cholinesterase activity, leading to health complications including damage to the nervous system and respiratory disorders [6-8]. Such outcomes pose a significant risk to food safety and public health [9, 10]. Therefore, it is imperative to develop a rapid, sensitive, and accurate method for detecting malathion residues to ensure food safety and preserve environmental and ecological integrity.

Current methods for detecting malathion predominantly utilise instrumental analyses, including gas chromatography (GC), high-performance liquid chromatography (HPLC), and gas chromatography-mass spectrometry (GC-MS) [11-14]. Although these techniques provide high detection accuracy and excellent separation, they also pose several challenges. These include the requirement for expensive equipment, complex operational procedures, lengthy detection cycles, and the necessity for skilled operators [15, 16]. Such limitations significantly impede their applicability for on-site rapid detection. In contrast, biosensor technology, which employs biological enzymes, has garnered attention due to its strong specificity and high sensitivity [17-19]. Nevertheless, core enzymes, such as acetylcholinesterase, are vulnerable to inactivation from environmental factors, including temperature and pH [20, 21]. Furthermore, the enzyme immobilisation process is complex, and stringent storage conditions are required, which restricts the widespread application of these biosensors in practical detection scenarios [22-26].

Enzyme-free sensors have become a prominent area of research in the detection of pesticide residues, owing to their numerous advantages, including stability, ease of preparation, low cost, and strong resistance to interference [27-30]. Nanoenzymes, which are a class of nanomaterials exhibiting enzyme-like catalytic activity, combine the catalytic properties of natural enzymes with the physicochemical stability of nanomaterials [31-33]. This combination presents promising applications in colourimetric sensing. Metal-organic framework (MOF) materials are often employed as carriers or active components ofnanoenzymes due to their high specific surface area, controllable pore structure, and abundant active sites [34-36]. Among these, UiO-66, a representative Zr-based MOF material, is recognised for its

exceptional chemical and thermal stability [37]. Its porous structure facilitates the effective dispersion of active components and mitigates agglomeration. Hemin, the active centre of hemoglobin, demonstrates peroxidase-like activity; however, its tendency to agglomerate when used in isolation limits its catalytic efficiency [38-40]. The incorporation of hemin into UiO-66 enhances its dispersibility via the MOF's porous structure and improves its catalytic performance through synergistic effects.

This study developed a Hemin@UiO-66 compositenanoenzyme and established an innovative enzyme-free colourimetric sensor for the detection of malathion. The research characterised the material's structure and morphology, thereby exploring both the peroxidase-like catalytic mechanism and the inhibition mechanism of malathion. Key parameters of the detection system were optimised to create a quantitative method for malathion detection. Subsequently, the sensor was applied to real sample analysis to validate its practical application, with the aim of providing a novel approach for the rapid detection of organophosphorus pesticide residues.

2 EXPERIMENTAL SECTION

2.1 Reagents and Instruments

Zirconium tetrachloride ($ZrCl_4$, 98%), terephthalic acid (H_2BDC, 98%), N,N-dimethylformamide (DMF, analytical grade), hemin (Hemin, 98%), 3,3',5,5'-tetramethylbenzidine (TMB, analytical grade), hydrogen peroxide (H_2O_2, 30%), malathion standard (97.4%), sodium hydroxide (NaOH, analytical grade), and sodium acetate (NaAc, analytical grade) were procured from Shanghai Macklin Biochemical Co., Ltd. Analytical-grade reagents, including absolute ethanol, dimethyl sulfoxide, and acetic acid, were obtained from Sinopharm Chemical Reagent Co., Ltd. Throughout the experiments, ultrapure water was employed.

The following instruments were utilised: X-ray diffractometer (XRD, D8 Advance, Bruker Corporation, Germany); Fourier transform infrared spectrometer (FT-IR, Nicolet iS50, Thermo Fisher Scientific, USA); scanning electron microscope (SEM, SU8010, Hitachi, Japan); ultraviolet-visible spectrophotometer (UV-Vis, UV-2600, Shimadzu Corporation, Japan); analytical balance (FA2004N, Shanghai Precise Scientific Instrument Co., Ltd.); ultrasonic cleaner (KQ5200DE, Kunshan Ultrasonic Instrument Co., Ltd.); vacuum drying oven (DZF-6050, Shanghai Jinghong Experimental Equipment Co., Ltd.); constant temperature magnetic stirrer (85-2, Shanghai Sile Instrument Co., Ltd.); and high-speed refrigerated centrifuge (TGL-16M, Hunan Xiangyi Laboratory Instrument Development Co., Ltd.).

2.2 Preparation of Hemin@UiO-66 Compositenanoenzymes

The synthesis of UiO-66 was optimised using a modified solvothermal method [41]. Specifically, 0.466 g of $ZrCl_4$ and 0.322 g of H_2BDC were accurately weighed and dissolved in 50 mL of DMF, employing 10 minutes of ultrasonic treatment. To adjust the pH, 6.0 mL of glacial acetic acid was incorporated into the solution. This mixture was subsequently transferred to a 100 mL polytetrafluoroethylene reactor and heated to 120 °C for 24 hours, followed by natural cooling to ambient temperature. The resultant product was centrifuged at 8000 rpm for 10 minutes, and the precipitate was collected. It was washed three times with both DMF and absolute ethanol to remove unreacted materials and impurities. Finally, the product was vacuum-dried at 80 °C for 12 hours, yielding purified UiO-66 powder, which was stored for future applications.

The post-modification method was utilised to synthesise Hemin@UiO-66. Initially, 50 mg of activated UiO-66 powder was measured and added to 10 mL of DMF solution. This mixture underwent ultrasonic dispersion for 15 minutes to achieve a homogeneous suspension. In a separate procedure, 20 mg of Hemin was weighed and dissolved in 20 mL of DMF. A 0.1 mol/L NaOH solution was added dropwise until the solution became clear. Subsequently, ultrasonic treatment was applied for 20 minutes to produce a Hemin-DMF solution. The two solutions were combined and magnetically stirred at low speed in the dark at room temperature for 24 hours. Following the reaction, the solution was centrifuged at 8000 rpm for 10 minutes, and the precipitate was collected. This precipitate was washed alternately with DMF and absolute ethanol three times to eliminate any unbound free Hemin, and then vacuum-dried at 60 °C for 12 hours. The resulting dark-brown Hemin@UiO-66 compositenanoenzyme solid was stored in a sealed container, protected from light, and refrigerated.

2.3 Peroxidase-like Activity and Detection Principle

To prepare a 3 mL reaction system, begin by adding 2420 μL of a 0.1 mol/L acetic acid-sodium acetate buffer, maintaining a pH of 4.0. Next, introduce 240 μL of a 10 mmol/L TMB solution, followed by the addition of 240 μL of a 50 mmol/L H_2O_2 solution. Subsequently, incorporate 100 μL of a 1 mg/mL Hemin@UiO-66 suspension. Ensure that the components are mixed thoroughly and allow the reaction to proceed at room temperature for 20 minutes. A blank control should be established using a system devoid of Hemin@UiO-66. Finally, record the absorption spectra from 450 to 750 nm using a UV-Vis spectrophotometer. The change in the characteristic absorption peak of oxTMB at 652 nm will indicate the peroxidase-like activity of Hemin@UiO-66.

2.4 Catalytic Kinetics of Hemin@UiO-66nanoenzyme

To investigate the catalytic kinetic mechanism of Hemin@UiO-66, a dual-substrate reaction system was employed to ascertain its catalytic kinetic parameters for H_2O_2 and TMB. The initial reaction rate (v) was determined by monitoring the change in intensity of the oxTMB absorption peak at 652 nm over time. The reaction rate was assessed by systematically varying the concentrations of TMB and H_2O_2. By applying the Michaelis-Menten equation, a plot of substrate concentration ([S]) against the initial reaction rate (v) was generated. The Lineweaver-Burk double-reciprocal method was utilised to fit the curve. The Michaelis constant (Km) and the maximum reaction rate (V) were calculated to evaluate the affinity and catalytic efficiency of Hemin@UiO-66 for both substrates.

2.5 Optimization of Detection Conditions

To achieve optimal detection performance, Single-factor optimisation was conducted of the key parameters within the reaction system. Firstly, we optimised the reaction time. With the optimal pH and temperature established, absorbance was measured at intervals of 5, 10, 15, 20, 30, and 40 minutes to determine the most suitable reaction duration. Next, we optimised the reaction temperature. We maintained all other conditions constant while varying the reaction temperatures at 20 °C, 30 °C, 40 °C, 50 °C, 60 °C, and 70 °C. This approach allowed us to assess the impact of temperature on the catalytic activity of thenanoenzyme. We then proceeded to optimise the pH. Acetic acid-sodium acetate buffer solutions were prepared at pH levels of 3.0, 3.2, 3.4, 3.6, 3.8, 4.0, 4.2, and 4.4. By keeping all other experimental conditions constant, we measured the system's relative activity at 652 nm for each pH level. Finally, we optimised the dosage of Hemin@UiO-66. The dosages of the Hemin@UiO-66 suspension were set at 20, 25, 30, 35, 40, 45, 50, and 55 μg/mL, while other conditions remained unchanged. This investigation aimed to elucidate the influence of material dosage on the detection efficacy.

2.6 Preparation of the Standard Curve

Under optimised experimental conditions, standard solutions of malathion at varying concentrations (0, 5, 15, 30, 60, 90, 120, 150, 180, 210, 240, 270 ng/mL) were introduced into the reaction system. For each concentration, three parallel experiments were performed. Following the reaction, absorbance was measured at 652 nm, and a standard curve was constructed. A quantitative detection equation was established through linear regression analysis. Subsequently, the method's limit of detection (*LOD*), calculated as 3σ/S—where σ represents the standard deviation of the blank samples and S denotes the slope of the standard curve—was determined.

2.7 Selectivity, Stability, Repeatability, and Anti-Interference Tests

In the selectivity experiment, several common pesticides were selected as potential interferents: prochloraz, acetochlor, imidacloprid, glufosinate-ammonium, lambda-cyhalothrin, chlorpyrifos, dichlorvos, dimethoate, and bispyribac-sodium. Solutions of these interferents were prepared at a concentration of 150 ng/mL. Each group underwent three parallel tests to ensure reliability. The effect of these interferents on the system's absorbance was evaluated using the detection method previously described. To assess the sensor's selectivity for malathion, the relative activity was calculated.

Stability Experiment: The Hemin@UiO-66 suspension was prepared, sealed, and stored in a refrigerator at 4 °C. Samples were collected at 0, 5, 15, 20, 30, and 40 days. Three parallel tests were performed for each time point. The catalytic activity and relative activity towards 150 ng/mL malathion were evaluated using a standard method to assess the material's storage stability.

Repeatability Experiment: Perform six independent parallel detections using a 150 ng/mL malathion standard solution as the target under optimised experimental conditions. For each group, establish three parallel tests. Measure the absorbance at 652 nm for each detection. Subsequently, calculate the relative standard deviation (RSD) of the absorbance values to evaluate the repeatability and reliability of the detection method.

Anti-interference Experiment: In a reaction system containing 150 ng/mL of malathion, 150 ng/mL of each interfering substance was introduced. The interfering substances comprised inorganic ions, including Na^+, K^+, Ca^{2+}, Mg^{2+}, and Cl^-, alongside common components of grain matrices such as starch, glucose, fructose, vitamin B, and glutamic acid. Three parallel experiments were conducted for each group. The absorbance was measured at 652 nm, and the relative activity was subsequently calculated. These results were then compared to those obtained from a system devoid of interfering substances, thereby evaluating the sensor's anti-interference capability.

2.8 Detection of Real Samples

Wheat and rice samples were employed stored as reserve grains in a grain depot as actual samples. The pretreatment followed the national standard (GB 23200.8-2016).We weighed 20.0 g homogenised sample and added 40 mL acetonitrile, vortexing 30 min. 5 g magnesium sulfate and 2 g sodium chloride, shake vigorously for 10 min. Centrifuged at 8000 rpm for 10 min.10 mL aliquot was evaporated under nitrogen at 50 °C and dissolved in 1 mL 0.1 mol/L acetic acid-sodium acetate buffer (pH = 4.0) and filtered through 0.22 μm filter membrane.

The recovery experiment utilised the standard addition method. Malathion standard solutions at three concentration levels—30 ng/mL, 90 ng/mL, and 180 ng/mL—representing low, medium, and high concentrations, were introduced to the treated sample solutions. The determination was conducted in accordance with the optimised detection method. For

each concentration level, three sets of parallel experiments were performed, and the spiked recovery rate, along with the relative standard deviation (RSD), was calculated.

3 RESULTS AND DISCUSSION

3.1 Material Characterization and Analysis

3.1.1 SEM analysis

Figure 1 shows scanning electron microscopy (SEM) images of Hemin, UiO-66, and Hemin@UiO-66 and EDS results of Hemin@UiO-66. Hemin (Figure 1) has irregular 3D aggregate shape without crystal structure. Its particle size distribution is uneven and its boundary is poorly defined due to amorphous agglomeration due to -stacking and hydrogen bonding between porphyrin compounds, typical of bulk Hemin material. However, UiO-66 (Figure 1) has irregular 3D aggregate shape with well defined outline, smooth surfaces and effective particle dispersion, consistent with characteristic crystal shape of UiO-66 metal-organic structure. In contrast, the synthesized UiO-66 has a highly ordered crystal structure.

In the SEM image of the Hemin@UiO-66 composite (Figure 1c), many octahedral UiO-66 particles are effectively integrated into the irregular flake substrate of Hemin, which has a high dispersion rate (no accumulation) and are firmly attached to the flake substrate.This composite structure of particles adhered to the flake substrate confirms that both materials have been successfully combined and are stable. Furthermore, it exposes active sites of UiO-66 and electrons are transported through Hemin's -conjugated system and thus provide a strong foundation for peroxidase activity.

The EDS energy spectrum and elemental map (Figure. 1d-k) show that Hemin@UiO-66 contains six elements: carbon (C), nitrogen (N), oxygen (O), zirconium (Zr), iron (Fe), and chlorine (Cl). Zr is assigned to UiO-66, Fe and Cl are the latter. Each element is evenly distributed across the surface and no accumulation occurs. The mass fractions correspond to the expected loading ratios and no spikes suggesting impurities are detected. We conclude that Hemin and UiO-66 are a homogenous composite rather than a physical mixture providing microscopic structural foundation for catalytic detection performance.

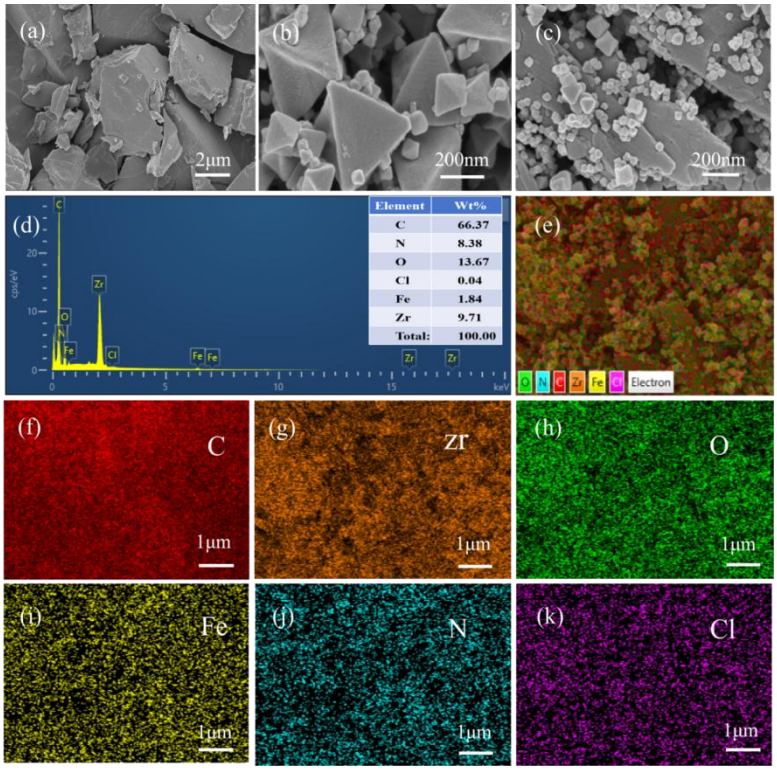

Figure 1 Presents SEM Images of Hemin, UiO-66, and Hemin@UiO-66, along with the EDS Spectrum Analysis Results for Hemin@UiO-66

3.1.2 Analysis of XRD and FT-IR

Figure 2 shows the XRD patterns for Hemin, UiO-66 and Hemin@UiO-66. UiO-66 has peak at 2 values 7.37°, 8.49°, 12.06°, 14.83°, 17.07° and 25.70° which indicates successful synthesis and high crystallinity [42]. Hemin has peak at 6.78°, 8.71°, 9.77°, 11.47°, 21.54°, 24.10° and 29.80° typical for porphyrin compounds [43].

The characteristic diffraction peaks of UiO-66 are not altered but are smaller in intensity. This is due to Hemin inhabiting pores of UiO-66 partially hiding crystallinity. The characteristic diffraction peaks of Hemin are absent, indicating Hemin is uniformly distributed at molecular level across the surface and pores of UiO-66 without forming aggregates. This distribution is consistent with the loading mechanism of physical adsorption and coordination bonding.

Figure 3 is the FTIR spectrum of UiO-66, Hemin, and Hemin@UiO-66. Strong absorption peaks between 1000 and 1500 cm-1 correspond to H2-BDC C=C and C-O stretching vibrations, and high absorption peaks between 500 and 1000 cm-1 correspond to Zr-O stretching vibrations [44] .Wide peaks between 3300 and 3500 cm-1 correspond to O-H bond stretching vibrations (-NH2) and adsorbed water. These peaks correspond to the infrared characteristics of UiO-66. The spectrum of Hemin shows absorptions between 1000 and 1400 cm-1, due to the skeletal vibrations of the porphyrin ring, and absorptions between 500 and 900 cm-1, due to the Fe-N bond stretching vibration between the porphyrin ring and Fe3+, and absorption peak between 1650 cm-1, due to the C=O stretching vibration characteristic of Hemin. In Hemin@UiO-66, both characteristic absorptions of UiO-66 and Hemin are present. The vibrations of UiO-66 are maintained between 1000 and 1500 cm-1, while Fe-N bond characteristic vibration peak remains between 500 and 900 cm-1. The intensity of O-H stretching vibration peak between 3000 and 3500 cm-1 is much larger than pure UiO-66. These results suggest Hemin has been successfully integrated into UiO-66 without loss of structure.

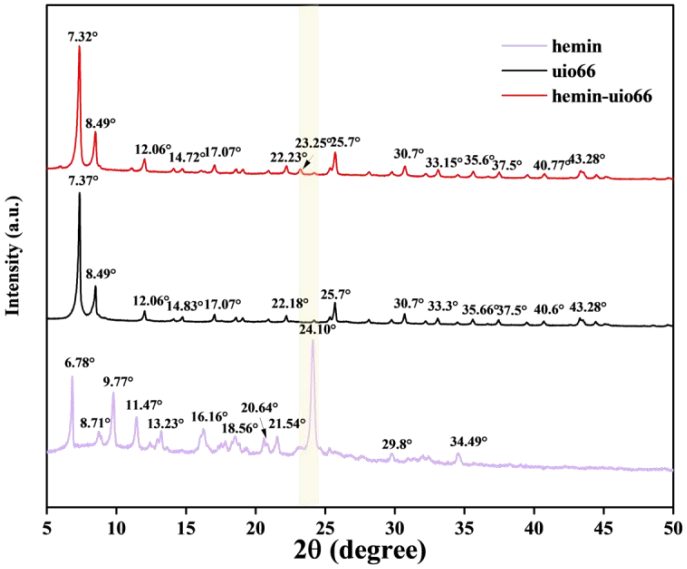

Figure 2 XRD Patterns of Hemin, UiO-66, and Hemin@UiO-66

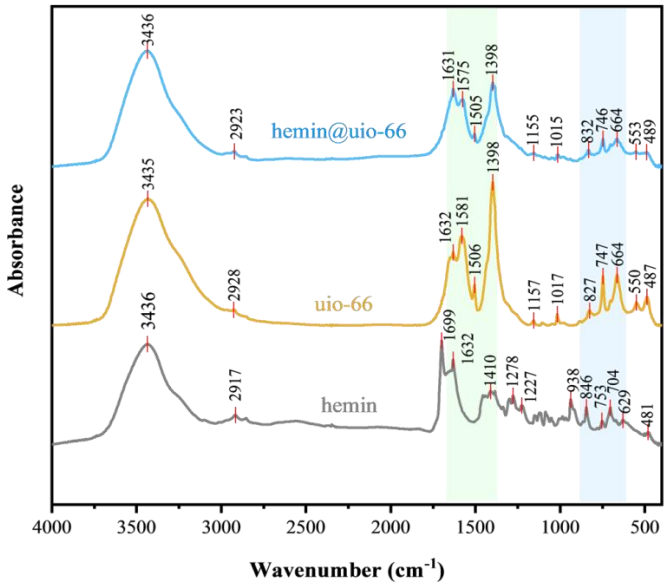

Figure 3 FT-IR Spectra of UiO-66, Hemin, and Hemin@UiO-66

3.1.3 XPS analysis

XPS was used to study the composition, chemical states and bonding properties of Hemin@UiO-66 composite, and study interaction between Hemin and UiO-66. The results are shown in Figure 4. Figure 4 shows full-spectrum XPS of Hemin@UiO-66 with C, N, O, Zr and Fe elements. C, N and O are mostly obtained from UiO-66 molecules and UiO-66 ligands, Zr is obtained from metal nodes of UiO-66 and Fe is obtained from the Hemin molecules. This shows that Hemin has successfully been integrated into the composite without any impurities, consistent with the preparation process.

Figure 4b shows the high resolution XPS spectrum of C 1s, which can be split into four peaks: 283.96 eV for the sp3-hybridised C-C bond, 284.80 eV for the sp2-hybridised C=C bond (benzene ring carbon), 286.36 eV for the C-O bond

(hydroxyl carbon) and 289.60 eV for the C=O bond (carboxyl carbon). The peak intensities of C-O and C=O bonds are significantly higher than pure UiO-66. This implies that the oxygen-containing functional groups of Hemin molecules interact with UiO-66 surface, resulting in more oxygen-containing carbon species.

Figure 4c shows the high resolution spectrum of N 1s divided into four distinct peaks: 397.92 eV for pyrrolic N, 399.34 eV for pyridinic N, 400.38 eV for graphitic N and 401.75 eV for protonated N. These nitrogen species arise from the porphyrin ring of Hemin without any new nitrogen chemical states, suggesting that the porphyrin structure of Hemin is retained during loading.

Figure 4e shows the high resolution XPS spectrum of Fe 2p. The highest peak at 712.5 and 725.8 eV are Fe 2p3/2 and Fe $2p_{1/2}$ respectively and the highest satellite peak at 718.5 and 732.1 eV. These results indicate that Fe^{3+} is the valence element in Hemin. The chemical environment of Fe^{3+} remains mostly unchanged after loading, eliminating the possibility of reduction or oxidation.

Figure 4f shows the high resolution spectrum of Zr 3d.peaks at 182.62 eV and 184.99 eV correspond to Zr $3d_{5/2}$ and Zr $3d_{3/2}$, respectively, indicating Zr^{4+} valence state, corresponding to pure UiO-66. These peak are moved by about 0.2 eV towards higher binding energies than pure UiO-66, due to coordination bonds between O atoms in Hemin molecules and Zr4+ which decreases electron cloud density around Zr^{4+} and increase binding energy. This proves that Zr-O coordination between Hemin and UiO-66 is present.

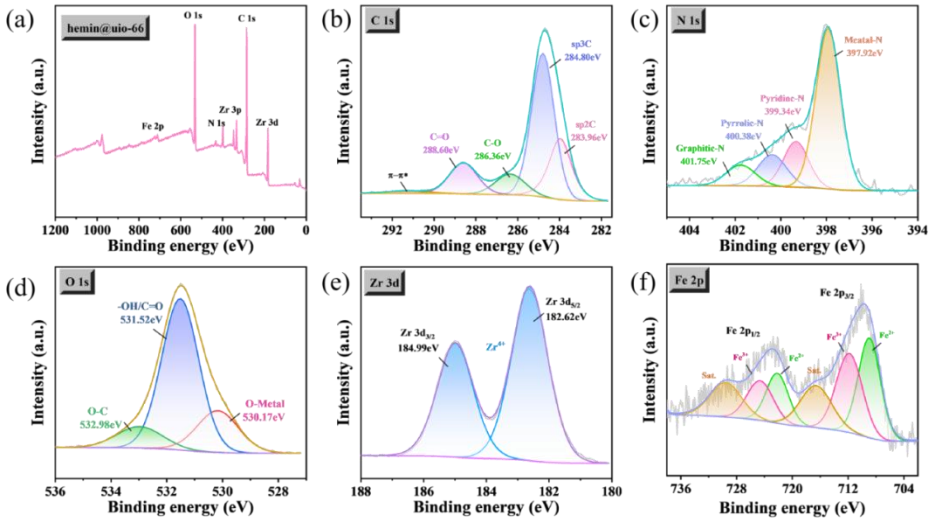

Figure 4 XPS Spectra of Hemin@UiO-66

In summary, the results from four characterization techniques—SEM-EDS, XRD, FT-IR, and XPS—corroborate one another, confirming the successful preparation of the Hemin@UiO-66 compositenanoenzyme. Additionally, the material exhibits a stable structure and uniform element distribution. A Zr-O coordination interaction between Hemin and UiO-66 underpins its peroxidase-like activity, providing both structural and chemical foundations.

3.2 Peroxidase-like Activity and Detection Principle

The peroxidase-like activity of Hemin@UiO-66 was confirmed through its ability to catalyze the oxidation reaction in the TMB-H_2O_2 system, as illustrated in Figure 5a. In the absence of Hemin@UiO-66, the blank system showed no significant absorption peaks between 450 and 750 nm, and the solution remained colorless. However, upon the addition of Hemin@UiO-66, a strong absorption peak emerged at 652 nm, and the solution rapidly turned blue. This indicates that Hemin@UiO-66 effectively catalyzes the decomposition of H_2O_2, producing hydroxyl radicals (· OH). These radicals further oxidize the colorless TMB, resulting in the formation of blue oxTMB, thereby demonstrating substantial peroxidase-like activity.

The effect of malathion on the catalytic activity of Hemin@UiO-66 is shown in Figure 5b. As the concentration of malathion increased, the absorbance value of the system at 652 nm gradually decreased, and the color of the blue solution gradually faded. The FT - IR characterization in Figure 5c shows that Hemin@UiO - 66 without the addition of malathion only exhibits the characteristic peaks of UiO - 66 and Hemin. After the adsorption of malathion, a new characteristic peak appears at 1048 cm^{-1}, corresponding to the stretching vibration of the P - O bond, which confirms the specific binding between malathion and Hemin@UiO - 66 [45].

The mechanism of action is as follows: The malathion molecule, which contains a phosphate group ($-PO_3^{2-}$), can coordinate with Zr^{4+} in Hemin@UiO-66 through Zr-O-P interactions. This adsorption on the material's surface occupies the active sites. Consequently, it obstructs H_2O_2 from binding to these sites, inhibiting the generation of ·OH and reducing the oxidation capability toward TMB. This leads to a decrease in oxTMB production and a decline in absorbance values. Utilizing this inhibitory effect, malathion can be quantitatively analyzed by detecting changes in the system's absorbance.

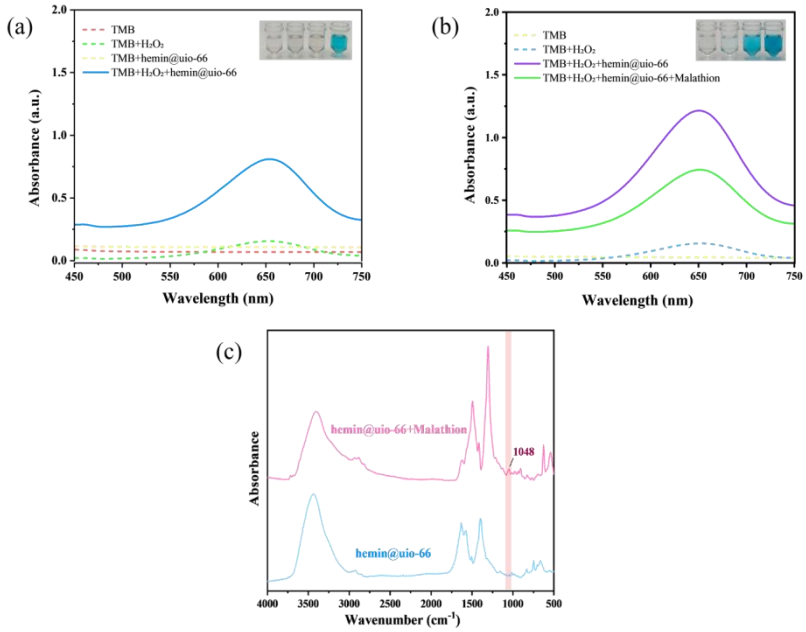

Figure 5 Presents the Following: (a) The UV-visible spectrum illustrating the peroxidase-like activity of Hemin@UiO-66, with an inset showing the color change in the reaction system; (b) The UV-visible spectrum depicting the inhibition of Hemin@UiO-66's peroxidase-like activity by malathion, accompanied by an inset of the reaction system's color change; (c) The FT-IR spectra of Hemin@UiO-66 before and after malathion adsorption

3.3 Catalytic Kinetics of Hemin@Uio-66nanoenzyme

To further explore the peroxidase-like catalytic properties of Hemin@UiO-66, we used H_2O_2 and TMB as substrates to examine its steady-state kinetic characteristics. The fitting results (Figure 6) demonstrate that the enzymatic reaction of Hemin@UiO-66 adheres to the Michaelis-Menten equation model. Additionally, the reciprocal of the reaction rate exhibits a linear relationship with the reciprocal of the substrate concentration, as shown in the double-reciprocal plot in Figure 6. The correlation coefficient $R^2 > 0.99$, indicating that the fitting results are highly reliable.

The kinetic parameters were determined using the Michaelis-Menten equation and the Lineweaver-Burk plot. For TMB as the substrate, the Michaelis constant (K_m) was 0.409 mM, and the maximum reaction rate (V_{max}) was 6.181×10^{-8} $M\cdot s^{-1}$. When H_2O_2 served as the substrate, K_m was 2.359 mM, and V_{max} was 5.427×10^{-8} $M\cdot s^{-1}$. These parameters, K_m and V_{max}, are essential for assessing enzyme catalytic ability: a lower Km signifies better enzyme-substrate affinity, while a higher V_{max} indicates a faster reaction rate and greater catalytic efficiency [46, 47].

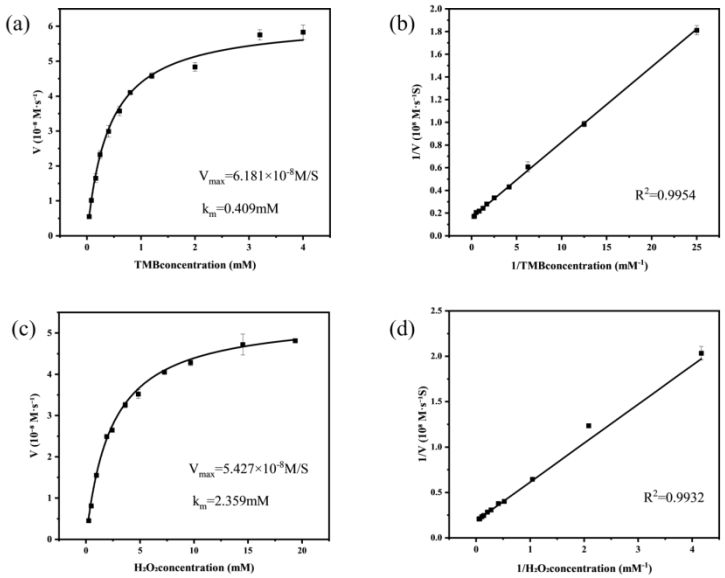

Figure 6 Illustrates the Catalytic Kinetics of Hemin@UiO-66 peroxidase-like activity. Panel (a) presents the Michaelis-Menten curve for TMB, while panel (b) shows the corresponding Lineweaver-Burk plot. Panel (c) depicts the Michaelis-Menten curve for H_2O_2, and panel (d) features the Lineweaver-Burk plot for H_2O_2

3.4 Optimization of Detection Conditions

Figure 7a shows the effect of *pH* on Hemin@UiO-66 catalytic activity and inhibition effect of malathion relative activity at 652 nm. The relative activity increases exponentially from 3.0 to 4.4, reaching 100% at 4.0, and decreasing steadily to 95% at 4.4. This is due to the impact of the proton concentration on the catalytic activity of the peroxidase-mimicking enzyme. Acidic conditions enhance the decomposition of H_2O_2 into OH, and high *pH* can lead to Fe^{3+} hydrolysis, decreasing Hemin catalytic efficiency, and Zr-O-P coordination. Therefore, 0.1 mol/L acetic acid-sodium acetate buffer was selectedat *pH* 4.0 as buffer medium.

Figure 7b demonstrates the effect of temperature on the detection system. From 20 °C to 50 °C, the relative activity is 95% stable. From 70 °C, the relative activity is 78% reduced due to the faster degradation of H_2O_2 at high temperature. More temperature can interfere with binding between Hemin and UiO-66. Room temperature (25 °C) is chosen for on-site applications.

Figure 7c shows the effect of reaction time on relative activity. Initially, between 5 and 20 minutes, relative activity increases rapidly with reaction time, and after 20 minutes, activity drops off, indicating that system is in dynamic equilibrium. We found that 20 minutes is the ideal reaction time, which allows catalytic efficiency and timely detection, and guarantees complete reaction progress and stable detection signal.

Figure 7d shows the effect of Hemin@UiO-66 dosage on detection effectiveness. As the dosage reaches 40 μg/mL, the relative activity of the system increases to 100% at 40 μg/mL. In addition, the relative activity decreases significantly, which indicates that the active sites of Hemin@UiO-66 are almost saturated at 40 μg/mL, and further dosage increases do not improve catalytic efficiency. Given detection sensitivity and cost, 40 μg/mL Hemin@UiO-66 is the optimal dosage.

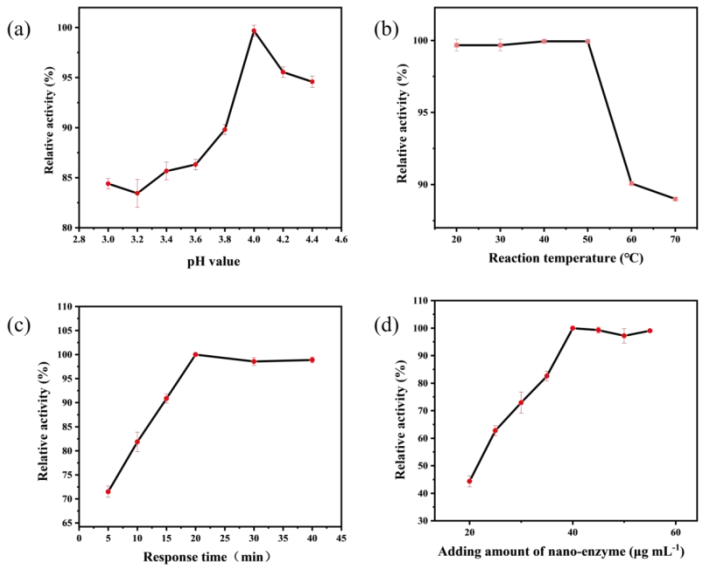

Figure 7 Illustrates the Impact of Various Experimental Conditions on the Reaction System: (a) *pH* value; (b) Reaction temperature; (c) Reaction time; (d) Quantity ofnanoenzyme added

3.5 Standard Curves and Limits of Detection

Under optimized experimental conditions, Figure 8 illustrates the relationship between malathion concentration and inhibition rate. A strong linear negative correlation exists between malathion concentrations ranging from 5 to 270 ng/mL and the system's absorbance. The linear regression equation is y = -0.00328x + 0.96412, with a correlation coefficient of R^2 = 0.996. The method's limit of detection, calculated as $3\sigma/S$, is 4.23 ng/mL, adequately meeting the detection requirements for trace malathion residues.

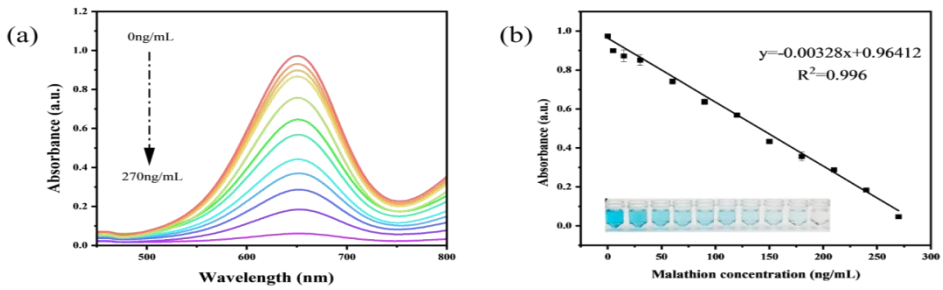

Figure 8 (a) UV-visible Absorption Spectra of the System with Varying Malathion Concentrations; (b) Calibration curve plotting absorbance against malathion concentration (Inset displays the color variations upon adding different malathion concentrations)

3.6 Selectivity, Stability, Repeatability, and Anti-interference Ability

3.6.1 Selectivity

Figure 9a shows how different interfering substances affect the colourimetric system. Most non-target pesticides such as prochloraz, acetochlor, imidacloprid, glufosinate-ammonium, lambda-cyhalothrin, chlorpyrifos, dichlorvos, dimethoate and bispyribac-sodium maintained the enzyme relative activity at about 90% (no deviations from the blank group), suggesting that these substances have no significant interference with the enzymatic activity. Malathion reduced enzyme relative activity to around 54% (indicating high specificity of malathion) and its ability to detect the enzyme for complex grain matrix.

3.6.2 Stability

The Hemin@UiO-66 was stored at 4 °C in a sealed container periodically and catalytic activity measured. Figure 9b shows 93% of its initial catalytic activity after 15 days and 88% after 40 days. This is a good storage stability. The RSD for each measurement was below 4.0%. This is due to the protective role of UiO-66 porous framework which prevents Hemin from accumulating and oxidising.

3.6.3 Repeatability

Using a 150 ng/mL malathion standard solution as the detection target, six parallel detections were conducted under optimized experimental conditions. The absorbance values at 652 nm were recorded, and the relative standard deviation (RSD) was calculated. As shown in Figure 9c, the RSD of the absorbance values from these six detections is 2.8%, which is below 5.0%. This demonstrates that the enzyme-free colourimetric sensor offers good reproducibility, with stable and reliable detection data, effectively minimizing errors from minor operational and instrumental fluctuations.

3.6.4 Anti-interference ability

Figure 9d shows the colourimetric system's strong resistance to interference from common grain matrix components. Even though it contains inorganic compounds such as Na^+, K^+, Ca^{2+}, Mg^{2+} and Cl, vitamins B and glutamic acid, starch, glucose, fructose and sodium chloride, the relative activity of the enzyme remains over 90%. It is not much different from the blank control group. These substances have little impact on the system. Only malathion inhibits the enzyme activity, decreasing its relative activity to about 53%. This confirms the enzyme's response to malathion, which shows that the enzyme can resist interference from common background substances when malathion is detected in complex grain matrices.

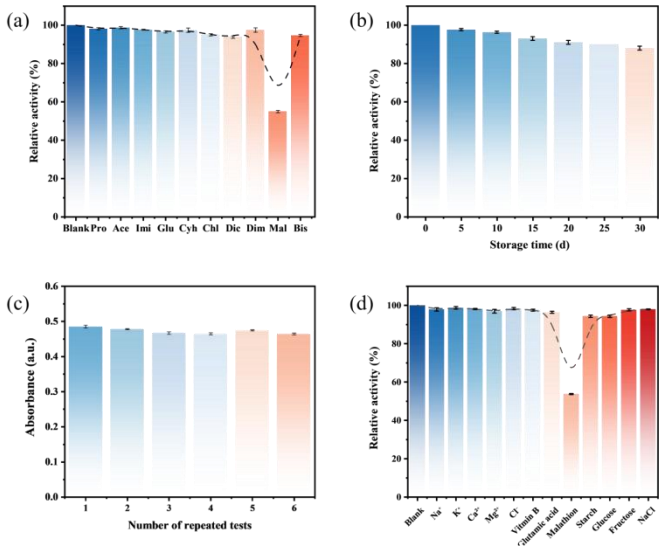

Figure 9 Illustrates Various Performance Metrics of the Colourimetric System for Detecting Malathion: (a) Selectivity, (b) Storage stability, (c) Repeated detection capability, and (d) Anti-interference ability

3.7 Detection of Real Samples

To evaluate its practical application, wheat and rice samples from a grain depot were selected for detection using standard addition method for recovery experiments. Samples were pre-treated according to the national standard method (GB 23200.8-2016). Standard addition concentrations were obtained from low (30 ng/mL), medium (90 ng/mL) and high (180 ng/mL). Each concentration was tested three times (Table 1). Recovery rates for standard additions ranged from 95.3% to 104.7% (RSD) with RSD between 2.1% and 4.2% (recovery rate 90%-150%,RSD 5%), which shows that the enzyme free colourimetric sensor can detect malathion residues in actual grain samples.

Table 1 Outcomes of the Spiked Recovery Experiment for Malathion in Real Samples (n = 3)

Sample	Added (ng/mL)	Found (ng/mL)	Recovery (%)	RSD (%)
Wheat	30.0	28.6±0.9	95.3	3.2
	90.0	91.9±3.1	102.1	3.4

Sample	Added (ng/mL)	Found (ng/mL)	Recovery (%)	RSD (%)
Rice	180.0	179.1±5.9	99.5	3.3
	30.0	29.4±0.6	98.0	2.1
	90.0	94.2±3.9	104.7	4.1
	180.0	181.8±7.6	101.0	4.2

4 CONCLUSIONS

We synthesized the Hemin@UiO-66 compositenanoenzyme which allows us to create enzyme-free colourimetric sensor for malathion detection. Thenanoenzyme benefits from the porous structure of UiO-66 and hence has uniform hemin dispersions, hence the peroxidase-like activity in the TMB-H2O2 system. Malathion inhibits the catalytic activity of thenanoenzyme by Zr-O-P coordination, which results in predictable changes of colour and absorbance. Under optimal conditions, the sensor has linear detection range 5 to 270 ng/mL and detection limit can be lowered to 4.23 ng/mL. It has excellent selectivity, stability and anti-interference capabilities. Tests on real grains show recovery rate between 95.3% and 104.7% with RSD of less than 4.2%, which meets the requirements for trace malathion residues.Unlike other methods, this sensor operates without biological enzymes, is easy to use, quick response and cost-effective. It presents a novel technique for rapid on-site detection of organophosphorus pesticide residues in food, with promising applications. Future work will focus on optimizing the Hemin@UiO-66 loading on cellulose test strips to develop a portable visual detection kit, and expanding the sensor to detect other organophosphorus pesticides.

COMPETING INTERESTS

The authors have no relevant financial or non-financial interests to disclose.

FUNDING

This work was supported by the Liquor Making Biological Technology & Application of Key Laboratory of Sichuan Province [grant number NJ2021-05]; Innovation and Entrepreneurship Training Program for College Students of Sichuan University of Science & Engineering [grant number cx2025011, cx2025132]; and the Innovation Fund of Postgraduate, Sichuan University of Science & Engineering [grant number D10503360].

AUTHOR CONTRIBUTION

Rui Liu: Conceptualization, Methodology, Data curation, Visualization, Writing - original draft. **Liang Dong:** Conceptualization, Funding acquisition, Project administration, Supervision, Writing-review & editing. **Wenjia Chen:** Validation, Conceptualization, Methodology. **Junxian Li:** Validation, Conceptualization, Methodology. **Run Wang:** Validation, Conceptualization, Methodology.

REFERENCES

[1] Mali H, Shah C, Raghunandan BH. Organophosphate pesticides an emerging environmental contaminant: pollution, toxicity, bioremediation progress, and remaining challenges. J. Environ. Sci., 2023, 127: 234-250.
[2] Serafim LF, Wang L, Rathee P, et al. Remediation of environmentally hazardous organophosphates by artificial metalloenzymes. Curr. Opin. Green Sustain. Chem., 2021, 32: 100529.
[3] Durgadevi P, Girigoswami K, Harini K, et al. Silent threats of organophosphates: surging pollutants, harmful impacts, remediation strategies, and viable eco-friendly alternatives. Toxicol. Environ. Health Sci., 2024, 17(1): 23 -49.
[4] Lamb RW, McAlexander H, Woodley CM, et al. Towards a comprehensive understanding of malathion degradation: theoretical investigation of degradation pathways and related kinetics under alkaline conditions. Environ. Sci. Process. Impacts, 2021, 23(8): 1231-1241.
[5] Kaushal J, Khatri M, Arya SK. A treatise on organophosphate pesticide pollution: current strategies and advancements in their environmental degradation and elimination. Ecotoxicol. Environ. Saf., 2021, 207: 111483.
[6] Lamb RW, McAlexander H, Woodley CM, et al. Towards a comprehensive understanding of malathion degradation: comparison of degradation reactions under alkaline and radical conditions. Environ. Sci. Process. Impacts, 2022, 24(7): 1026-1036.
[7] Liu Y, Xu Y, Yuan B, et al. Bioaccumulation mediated by water solubility leads to differences in the acute toxicity of organophosphorus insecticides to zebrafish (Danio rerio). Ecotoxicology, 2024, 33(7): 750-761.
[8] Ramadori GP. Organophosphorus poisoning: acute respiratory distress syndrome (ARDS) and cardiac failure as cause of death in hospitalized patients. Int. J. Mol. Sci., 2023, 24(8): 7168.
[9] Rafacho ML. Acute and chronic effects of the organophosphate malathion on the pancreatic α and β cell viability, cell structure, and voltage-gated K+ currents. Environ. Toxicol. Pharmacol., 2022, 94: 103929.
[10] Kaur R, Choudhary D, Bali S, et al. Pesticides: an alarming detrimental to health and environment. Sci. Total Environ., 2024, 915: 113-170.

[11] Wang C. Selective and sensitive detection of malathion pesticide with CdSe quantum dots as ligand-exchange probes. Environ. Eng. Sci., 2021, 38(10): 920-928.
[12] Khatoon R, Uddin R, Khurshid S, et al. Determination of lambda-cyhalothrin and malathion residues in locust by gas chromatography with electron capture detection. J. Anal. Chem., 2022, 77(5): 611-617.
[13] Michlig N, Amirav A, Neumark B, et al. Comparison of different fast gas chromatography-mass spectrometry techniques (Cold EI, MS/MS, and HRMS) for the analysis of pyrethroid insecticide residues in food. Anal. Methods, 2024, 16(32): 5599-5618.
[14] Garvey J, Margalit A, Kelly M, et al. A method for the quantitative analysis of polar anionic pesticides in milk/infant formula, cereals and fruit and vegetables using ion chromatography coupled to tandem mass spectrometry. Anal. Methods, 2024, 16(23): 3692-3700.
[15] Ziani I, Bouakline H, Guerraf AE, et al. Integrating AI and advanced spectroscopic techniques for precision food safety and quality control. Trends Food Sci. Technol., 2025, 156: 104850.
[16] Sestak J, Guttman A, Lavicka J. Fluorescence detection setups in capillary electrophoresis and microscale liquid chromatography: developments over the past decade. TrAC, Trends Anal. Chem., 2024, 181: 118001.
[17] Patel M, Agrawal M, Srivastava A. Signal amplification strategies in electrochemical biosensors via antibody immobilization and nanomaterial-based transducers. Mater. Adv., 2022, 3(24): 8864-8885.
[18] Marrazza G, Ramalingam M, Jaisankar A, et al. Advancements and emerging technologies in biosensors for rapid and accurate virus detection. TrAC, Trends Anal. Chem., 2024, 172: 117609.
[19] Altan EA. Nanomaterial interfaces designed with different biorecognition elements for biosensing of key foodborne pathogens. Compr. Rev. Food Sci. Food Saf., 2023, 22(4): 3151-3184.
[20] Zlobin A, Smirnov I, Golovin A. Dynamic interchange between two protonation states is characteristic of active sites of cholinesterases. Protein Sci., 2024, 33(2): e4894.
[21] Alves AA, Furtado DA, de Oliveira RR, et al. Mechanisms of organophosphate toxicity and the role of acetylcholinesterase inhibition. Toxics, 2023,11(6): 512.
[22] Holyavka MG, Artyukhov VG. Prospects and problems in enzyme immobilization methodology: comprehensive review. Biophys. Rev., 2025.
[23] Shahbaz A, Hussain N, Intisar A, et al. Immobilized enzymes-based biosensing cues for strengthening biocatalysis and biorecognition. Catal. Lett., 2021, 152(9): 2637-2649.
[24] Bolivar JM, Woodley JM, Fernandez-Lafuente R. Is enzyme immobilization a mature discipline? Some critical considerations to capitalize on the benefits of immobilization. Chem. Soc. Rev., 2022, 51(15): 6251-6290.
[25] Jiang Y, Zheng J, Wang M, et al. Pros and cons in various immobilization techniques and carriers for enzymes. Appl. Biochem. Biotechnol., 2024, 196(9): 5633-5655.
[26] Bie J, Sepodes B, Ribeiro MHL. Enzyme immobilization and co-immobilization: main framework, advances and some applications. Processes, 2022, 10(1): 1-20.
[27] Karadurmus L, Kaya IS, Ozkan SA. Recent advances of enzyme biosensors for pesticide detection in foods. J. Food Meas. Charact., 2021, 15(5): 4582-4595.
[28] Abedeen MZ, Sharma M, Kushwaha HS, et al. Sensitive enzyme-free electrochemical sensors for the detection of pesticide residues in food and water. TrAC, Trends Anal. Chem., 2024, 176: 117729.
[29] Majdinasab M, Daneshi M, Marty JL. Recent developments in non-enzymatic (bio)sensors for detection of pesticide residues: focusing on antibody, aptamer and molecularly imprinted polymer. Talanta, 2021, 232: 122397.
[30] Praharaj C, Nara S. Nanotechnology driven biorecognition element and label free sensing of pesticides. J. Environ. Chem. Eng., 2024, 12(2): 112168.
[31] Jeyachandran S, Srinivasan R, Ramesh T, et al. Recent development and application of nanozyme artificial enzymes-a review. Biomimetics, 2023, 8(5): 1-20.
[32] Bilal M, Khaliq N, Ashraf M, et al. Enzyme mimic nanomaterials as nanozymes with catalytic attributes. Colloids Surf. B: Biointerfaces, 2023, 221: 112950.
[33] Abdullah KA, Tahir TF, Qader AF, et al. Nanozymes: classification and analytical applications - a review. J. Fluoresc., 2024, 34(5): 1987-2004.
[34] Cedrun-Morales M, Ceballos M, Polo E, et al. Nanosized metal-organic frameworks as unique platforms for bioapplications. Chem. Commun., 2023, 59(20): 2887-2896.
[35] Wang D, Yao H, Ye J, et al. Metal-organic frameworks (MOFs): classification, synthesis, modification, and biomedical applications. Small, 2024, 20(47): 2404350.
[36] Udourioh GA, Solomon MM, Matthews-Amune CO, et al. Current trends in the synthesis, characterization and application of metal-organic frameworks. React. Chem. Eng., 2022, 8(2): 278-310.
[37] Zhao R, Scott TR, Schmid J, et al. Cross-aldol condensation on missing linker sites of metal-organic framework UiO-66. J. Catal., 2025, 448: 116204.
[38] Guo J, Liu Y, Zha J, et al. Enhancing the peroxidase-mimicking activity of hemin by covalent immobilization in polymer nanogels. Polym. Chem., 2021, 12(6): 866-858.
[39] Sun H, Wu H, Teng Q, et al. Enzyme-mimicking materials from designed self-assembly of lysine-rich peptides and G-quadruplex DNA/hemin DNAzyme: charge effect of the key residues on the catalytic functions. Biomacromolecules, 2022, 23(8): 3476-3489.
[40] Lai S, Yang D, Wang Y, et al. Artificial peroxidase of short peptide and hemin co-assemblies with selective chiral catalytic activity in DOPA oxidation. Colloids Surf. A: Physicochem. Eng. Asp., 2023, 665: 131257.

[41] Cunha-Silva AV, de Sousa IR, de Oliveira LG, et al. Influence of UiO-66(Zr) preparation strategies in its catalytic efficiency for desulfurization process. Materials, 2019, 12(10): 1610.
[42] Richezzi M, Donnarumma RP, Howarth AJ. Developments in the discovery, synthesis, and characterization of RE(III)-UiO-66 and its structural analogues. CrystEngComm, 2025, 27(8): 1062-1075.
[43] Li Z, Deng X, Hong X, et al. Nanozyme based on dispersion of hemin by graphene quantum dots for colourimetric detection of glutathione. Molecules, 2022, 27(15): 1-12.
[44] Chen S, Guo J, Sun Q, et al. Enhanced electrochemical sensor based on Uio-66-NH2 carbon nanotubes hybrid for selective detection of ofloxacin. Mater. Today Chem., 2024, 42: 102441.
[45] Li X, Liu P, Niu X, et al. Tri-functional Fe-Zr bi-metal-organic frameworks enable high-performance phosphate ion ratiometric fluorescent detection. Nanoscale, 2020, 12(37): 19383-19389.
[46] Aledo JC. Enzyme kinetic parameters estimation: a tricky task? Biochem. Mol. Biol. Educ., 2021, 49(4): 514-515.
[47] Dong J. On catalytic kinetics of enzymes. Processes, 2021, 9(5): 1-8.